Metal-free dual-phase full organic carbon nanotubes/g-C_3N_4 heteroarchitectures for photocatalytic hydrogen production

Konstantinos C. Christoforidis[a,b,*], Zois Syrgiannis[a], Valeria La Parola[c], Tiziano Montini[a,d], Camille Petit[b], Elias Stathatos[e], Robert Godin[f], James R. Durrant[f], Maurizio Prato[a,g,h], Paolo Fornasiero[a,d,**]

[a] Department of Chemical and Pharmaceutical Sciences and INSTM Research Unit, University of Trieste, via L. Giorgieri 1, 34127 Trieste, Italy
[b] Barrer Centre, Department of Chemical Engineering and Barrer Centre, Imperial College London, South Kensington Campus, London SW7 2AZ, UK
[c] Istituto per lo Studio dei Materiali Nanostrutturati (ISMN-CNR), via Ugo La Malfa 153, I-90146 Palermo, Italy
[d] ICCOM-CNR Trieste Research Unit, University of Trieste, via L. Giorgieri 1, 34127 Trieste, Italy
[e] Department of Electrical Engineering, Technological Educational Institute (TEI) of Western Greece, 26334 Patras, Greece
[f] Department of Chemistry and Centre for Plastic Electronics, Imperial College London, South Kensington Campus, London SW7 2AZ, UK
[g] Carbon Nanobiotechnology Laboratory, CIC biomaGUNE, Paseo de Miramón 182, San Sebastian, Spain
[h] Basque Fdn Sci, Ikerbasque, Bilbao 48013, Spain

ARTICLE INFO

Keywords:
Hydrogen
Carbon nitride
Photocatalysis
Carbon nanostructures
Carbon nanotubes
Renewable energy

ABSTRACT

Hydrogen generation from water using solar energy has grown into a promising approach for sustainable energy production. Over the last years, graphitic carbon nitrides (g-C_3N_4, CN), polymers based on the heptazine-group, have been widely applied as photocatalysts for H_2 evolution. The poor charge separation efficiency of CN is considered the major drawback. Here, we investigated the effect of coupling CN with different types of carbon nanotubes on the charge transfer properties and the photocatalytic H_2 evolution. We used carbon nanotubes (CNTs) of different wall number (single (SWCNTs), double (DWCNTs) and multi-walled (MWCNTs) CNTs) for the development of full-organic CN based composite photocatalysts. Photoactivity was drastically affected by the content but more importantly by the nature of the CNTs. The SWCNTs functionalized CN composites were the most active presenting approximately 2–5 times higher H_2 evolution than the corresponding DWCNTs and MWCNTs functionalized CN under both solar and pure visible light irradiation. Photoactivity was primarily controlled by the improved electronic properties linked with the abundance and stability of photogenerated charges as evidenced by electron paramagnetic resonance spectroscopy. Transient absorption spectroscopy verified the transfer of reactive electrons from CN to CNTs. CNTs functioned as electron acceptors improving charge separation. The data suggest that charge transfer is inversely proportional to the wall number of the CNTs and that photoactivity is directly controlled by the size at the nanoscale of the CNTs used. In the CNTs/CN nanocomposites, photogenerated electrons are transferred more efficiently from CN when SWCNTs are used, providing more available electrons for H_2 production.

1. . Introduction

The ability to provide a sustainable supply of clean energy is one of the most critical challenges of our society. This is related a) to the negative environmental impact of the use of fossil fuels, with the release of pollutants and greenhouse gases such as CO_2, and b) to the progressive depletion of their reserves. In addition, the increasing demand of energy forces the development of alternative approaches for the production of clean and renewable energy. In this regards, photocatalytic hydrogen production using semiconductors is considered one of the viable strategies to deal with both energy supply and environmental issues [1,2]. H_2 can be efficiently used in Fuel Cells producing only H_2O while the use of the renewable and largely available solar energy for its production offers additional benefits in terms of sustainability.

Numerous semiconductors including metal sulfides [3], metal oxides [4] or even organic nanomaterials [5,6] have been proven able to produce H_2 under sunlight or visible light. Among them, the

* Corresponding author at: Barrer Centre, Department of Chemical Engineering and Barrer Centre, Imperial College London, South Kensington Campus, London SW7 2AZ, UK.
** Correspondence to: Department of Chemical and Pharmaceutical Sciences, University of Trieste, via L. Giorgieri, 1, 34127 Trieste, Italy.
E-mail addresses: kchristofo@gmail.com (K.C. Christoforidis), pfornasiero@units.it (P. Fornasiero).

Accepted 29 May 2018

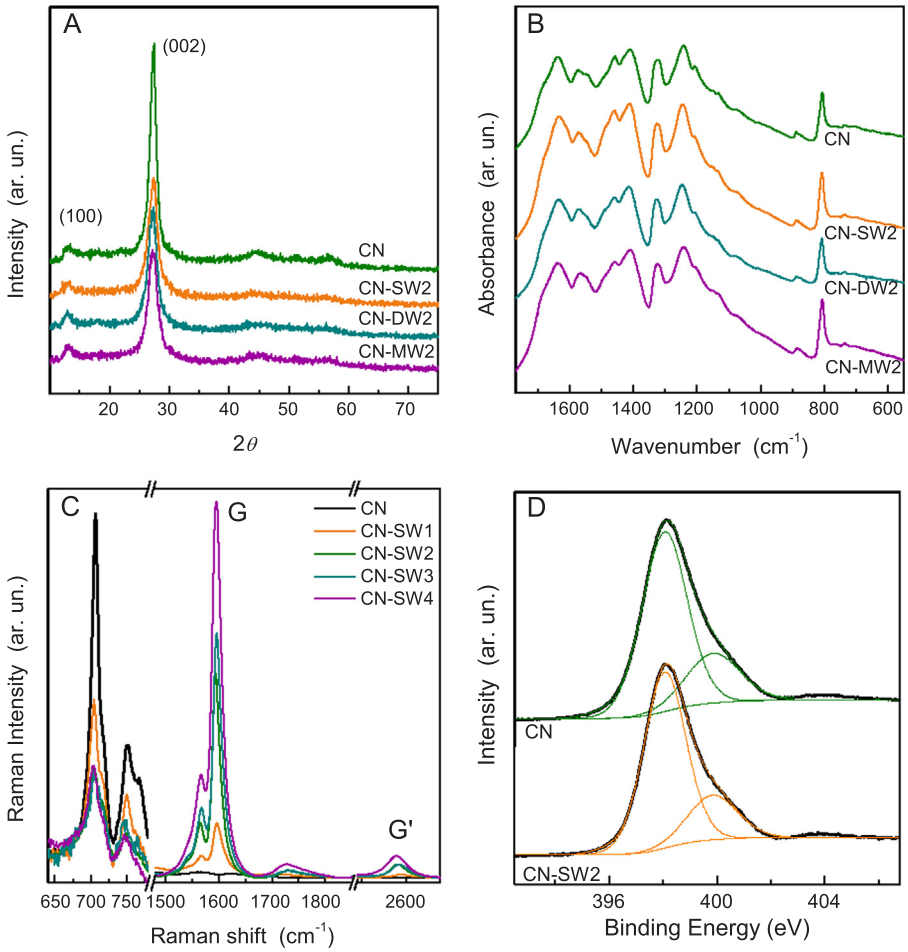

Fig. 1. A) XRD patterns of the pure CN and CNTs/CN nanocomposites. For the sake of comparison, the intensity of the CN pattern presented is divided by a factor of 2. B) FT-IR absorption spectra of the pure CN and the nanocomposites containing CNTs of different wall number. C) Raman spectra of the pure CN and the nanocomposites containing different SWCNTs content recorded using a laser of λ_{exc} = 785 nm showing the characteristic peaks of both CN and SWCNTs. D) High-resolution N 1s XPS spectra of the reference CN sample and the CN-SW2 composite. Materials labeling: CN-Y*x* where Y indicates the CNTs used (e.g. SW for SWCNTs, DW for DWCNTs and MW for MWCNTs) and the increasing *x* value denotes samples with increasing CNTs content. CN stands for the pure carbon nitride.

polymeric semiconductor graphitic-like carbon nitride (g-C_3N_4, CN) is considered a promising candidate for hydrogen production [5,7]. It is an earth-abundant, metal-free, non-toxic and low-cost photocatalyst containing only carbon, nitrogen and hydrogen atoms. Furthermore, CN has high chemical stability under working conditions, relatively low band gap energy (E_g of 2.7 eV) and suitable band edge potential level for proton reduction. Its polymeric nature permits modification of its textural properties and morphology [2,8] as well as functionalization with heterostructures [9]. However, inherent drawbacks such as fast recombination rates of the photogenerated charges result in moderate photoactivity of pure or bulk CN [10–12]. Studies have shown that the synthesis conditions can strongly affect the electronic and optical properties and therefore the catalytic activity of CN [13,14]. To overcome these intrinsic limitations, different strategies have been employed over the last years including doping with metallic and non-metallic elements [15], hard and soft templating techniques to control porosity and shape [16,17], control of morphology [14] and coupling with inorganic [9,18] and organic [19] nanostructures for the development of heterojunctions and heterostructures. In particular, significant progress has been achieved in the coupling of CN with carbon nanostructures such as graphene [20,21], carbon dots [22,23], C_{60} [24], carbon nanospheres [25] and carbon nanotubes (CNTs) [26–33]. In this type of materials, studies made use of the unique carbon nanostructures properties such as the high electron reservoir ability and high conductivity, allowing increased photogenerated charge separation. This has been ascribed to their π-conjugated structure [19,34].

CNTs have received great attention for applications in various catalytic reactions due to their morphology, high surface area and great electronic conductivity [35,36]. Multi-walled CNTs have been used and coupled with bulk [26], mesoporous [28] and CN nanosheets [27], through in-situ [29,37] but also two-pot synthesis approaches [27] with interesting perspectives for photocatalytic H_2 production. Typically, functionalized CNTs have been used, mostly by simply oxidizing the CNTs [30]. Generally, the observed enhanced H_2 photo-production was attributed to an increased charge separation efficiency due to the presence of the carbon nanostructure [28]. Morphological changes in CN induced by the presence of CNTs may also contribute to the final photocatalytic activity [29]. This has been linked with the CNTs amount used resulting in either fully incorporated CNTs within the CN sheets or even independently coiled and isolated CNTs [29]. Optimal CNTs content in the final composite is important to maximize the performances [31,32]. Although CN has been coupled with different carbon nanostructures, the effect of morphological parameters at the nanoscale, such as the thickness and size of carbon-based nanomaterials, has never been investigated.

Herein, inspired by the different electronic properties linked with the thickness of carbon nanomaterials (i.e. number of layers) as in the case of graphene-based materials [38], we synthesized a series of CNTs/CN nanocomposites through the coupling of CN with CNTs of different wall number. This was done in an effort to evaluate the CNTs nature on the electronic properties of the synthesized nanocomposites. 1-dimensional pristine SWCNTs, DWCNTs and MWCNTs were used for the development of the nanocomposites without addition of any other component. The specific surface area of the CNTs follows the trend SWCNT > DWCNT > MWCNT (ca. 1000, 500 and 110 m^2/g, respectively) and the conductivity follow the same trend (ca. 3390, 1880 and 1530 S/m, respectively) [39,40]. The diameter (1.2–1.7, 3.5 and 20–30 nm for SWCNT, DWCNT and MWCNT, respectively) and length follow the opposite trend (0.1–4, 1–10 and 10–30 μm for SWCNT, DWCNT and MWCNT, respectively). Nevertheless, electronic properties

are mostly defined by the wall number, as the length is for all materials in the micrometer range. At variance with previous studies, herein pristine instead of functionalized CNTs were used and the effect of the CNTs wall number is studied. The prepared CNTs/CN nanocomposites were applied for photocatalytic H_2 evolution and proven more active than pure CN. The SWCNTs/CN series showed the highest activity among all nanocomposites. The materials were fully characterized and the effect of CNTs content and nature is analyzed.

2. Results and discussion

The CNTs functionalized CN composites were obtained by in-situ formation of CN from melamine in the presence of pristine CNTs. The synthetic process takes advantage of the π-π interactions between melamine and CNTs, favoring a tight contact between the CNTs scaffold and the growing CN. Thermogravimetric analysis (Fig. S1) confirm the close contact between the component as the pristine CN begins to decompose at about 550 °C, while the process starts at lower temperature in all nanocomposites. The final CNTs loading obtained from TGA data (Table S1) is significantly higher than the nominal value, due to the mass loss during melamine thermal polycondensation process.

XRD and FT-IR spectroscopy were used to determine the structure and chemical features of the pristine CN and the CNTs/CN nanocomposite materials. Fig. 1A and S2 show the XRD patterns of the prepared materials. Two characteristic reflections were detected at approximately 2θ 13.0° and 27.3° corresponding to the (100) and (002) crystal planes of CN, e.g. the in-plane distance between nitride pores and the stacking of conjugated C_3N_4 layers respectively [41]. These results confirm the formation of the graphitic stacking structure. In addition, the decrease of the main reflection intensity at 27.3° in the presence of CNTs (note that the XRD pattern of the pristine CN in Fig. 1 is divided by 2) may suggest deviation in the interlayer stacking compared with the pristine CN [33,42]. This may originate from the incorporation of CNTs within the CN nanoplates framework and weaken the interlayer stacking force [24]. In all nanocomposites no reflections corresponding to the CNTs were detected, due to the low CNTs content (TGA). FT-IR spectra further confirmed the formation of CN (Fig. 1B and S3). All the characteristic peaks of CN were observed and no differences were detected comparing the pristine CN with the CNTs/CN nanocomposites. The sharp peak centered at 810 cm^{-1} is attributed to the *s*-triazine ring modes. The strong absorption bands in the 1200–1680 cm^{-1} region originate from the stretching vibration modes of heptazine heterocyclic ring (C–N–C) while the broadened band at high wavenumber (~ 3200 cm^{-1}) is attributed to the N–H stretching vibration (primary (–NH_2) and secondary (= N–H) amines) [5,43].

To further confirm the presence of CNTs in the nanocomposites, Raman spectroscopy was used due to the ability to identify the graphitic nature of carbon nanostructures. As illustrated in Fig. 1C and S4, the characteristic Raman bands of CN are not influenced by the presence of CNTs. In the case of SWCNTs and DWCNTs, the D- and G-bands (characteristic of sp^2-hybridized carbon networks) are clearly observed (Fig. 1C and S4A) [44,45]. For the MWCNTs/CN series, the characteristic CNTs bands are only observed for the high loaded samples (i.e. CN-MW3 and −4). Nevertheless, in all three series the intensity of the CNTs band increases with increasing CNTs content. These results clearly indicate that the structure of the CNTs is maintained during the thermal treatment for the development of the nanocomposites. In addition, a clear shift of the high frequency modes was detected when comparing the pristine CNTs with the nanocomposites (Fig. S5). Shifts like these have been previously assigned to charge transfer processes between CNTs and other components including CN [30,46,47] and strongly suggest the presence of a tight interaction between the CNTs and CN.

XPS analysis was performed on the CN, CN-SW2, CN-DW2 and CN-MW2 samples. N1s and C1s spectra of CN and CN-SW2 are shown in Fig. 1D and S6 respectively. C1s and N1s peaks of CN are typical of CN samples [33,42]. The C1s spectrum can be fitted with three components at 287.7 (due to sp2 carbon atoms bonded to N inside the aromatic structure), 284.1 and 285.7 eV (due to C=C bonds in aromatic structures and to C-OH bond arising from some surface contamination). In the composite materials the relative percentage due to nitride structure decreases and the component at 284.1 eV typical of the graphitic structure of carbon nanotube increases. The sample in which the CNT structure is more evident is the CN-SW2. If we observe the N1s region (Fig. 1D) we find the typical components found for CN, i.e. 398.1 eV (sp2 N atoms involved in triazine rings) and 399.8 eV (bridging N atoms in N-(C3) or N bonded with H atoms). The formation of the composite does not change the position and the relative intensity of the N1s peaks indicating that the in-plane tri-*s*-triazine basic unit is retained. Similar results appeared for the materials with DWCNTs and MWCNTs. Table S2 reports the relative amount of the different C1s and N1s species, showing a clear increase of the C-component corresponding to the graphitic structure of CNTs in the composites.

Nitrogen sorption isotherms were performed to study the textural properties of the materials (Fig. S7–9). All materials presented type IV isotherms with H3 hysteresis loop indicating the presence of a mesoporous structure, typical of CN [9]. Small differences in the three series were detected in the BET surface area and porosity. In the CN-SW*x* series, a small enhancement of the surface area was observed with increasing SWCNTs content. In the CN-DW*x* series, an enhancement was observed only for the high loaded CN-DW4 sample. On the contrary, no obvious change in surface area was detected for the CN-MW*x* samples. The low amount of CNTs may explain the non-proportional improvement in surface area with increasing CNTs [30]. Given the large surface area of CNTs, the relatively small values obtained for the composite may indicate that CNTs are well covered with CN nanosheets. The small increase of the surface area with increasing CNTs content also suggests the CNTs well coverage with CN and their incorporation within the CN nanoplates framework. The observed trend in surface area between the three series (CN-SW*x* > CN-DW*x* > CN-MW*x*) follows the surface area of the CNTs used. This may indicate that the increased surface area in the nanocomposites could originate from uncovered CNTs. The samples presented broad BJH pore size distribution (Fig. S10) and all composites showed a shift towards higher values compared to the pristine CN. The pore size distribution in the CN-SW*x* materials increased with increasing SWCNTs content which may originate from morphological changes induced by the incorporation of the CNTs in the CN structure. The CN-DW*x* and CN-MW*x* series presented a broad pore size distribution centered at 28 nm that did not vary with CNTs content.

The morphology of the prepared materials was investigated using TEM and AFM. The pure CN sample presents a layered and platelet-like structure, typical of CN while the CNTs morphology can be observed in the nanocomposites (Fig. 2 and S11). Moreover, CNTs are well dispersed and look like they are stacked within or wrapped by CN particles. This further confirms the presence of a tight interaction between CNTs and CN. In addition, the observed incorporation of the CNTs within the framework formed by the aggregation of irregular and some difference in the size of the CN particles can explain the small increase of the nanocomposites surface area and in particular those containing small amount of CNTs.

The addition of SWCNTs to CN significantly changed the dimensions of the graphitic features. As exemplified in Fig. 2, while both samples presented similar thickness distribution, the addition of the SWCNTs decreased the diameter of the graphitic features from some micrometers in the case of CN to some hundreds of nanometers for CN-SW2 and CN-DW2 (Fig. 2 and S11). This may originate from the incorporation of CNTs within the CN nanoplates framework and weaken the interlayer stacking or hydrogen bonding force resulting in smaller CN particles. Comparing the composites bearing CNTs of different wall number, the CN-DW2 and CN-MW2 samples presented thicker CN 2D structures.

The absorption edge of the pure CN material is around 450 nm, corresponding to a band-gap energy (E_g) of 2.84 eV (Fig. S12). For the

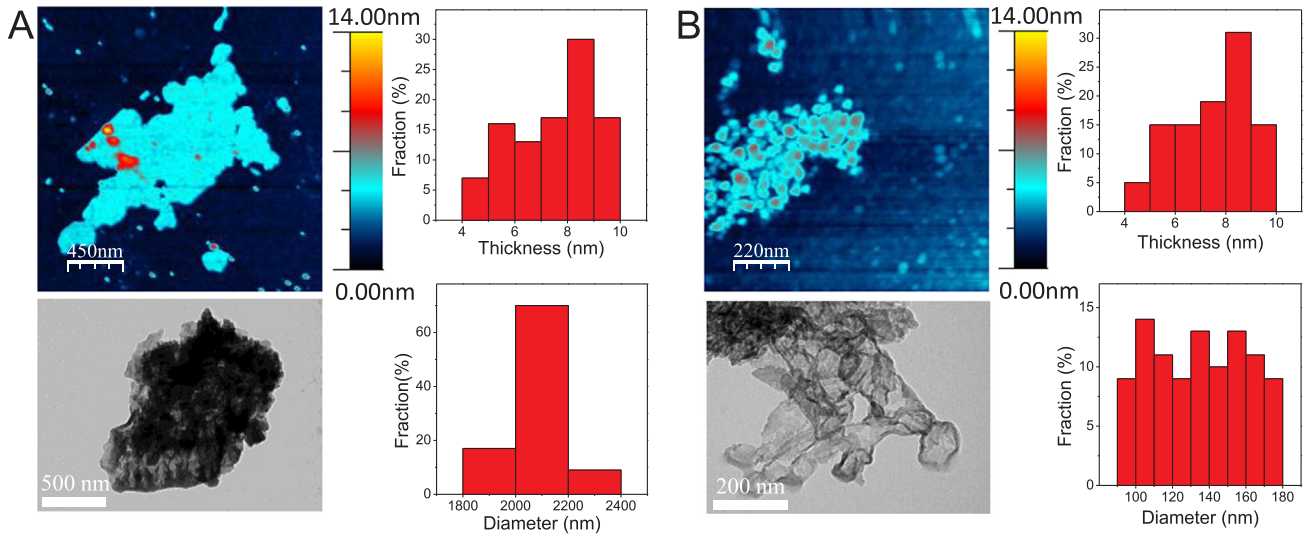

Fig. 2. AFM and TEM images and height and diameter distribution of the CN (A) and CN-SW2 (B) catalyst.

nanocomposites containing SWCNTs no obvious change in the E_g was observed while a small shift of the E_g towards lower values was detected in the nanocomposites containing MWCNTs and DWCNTs, i.e. E_g = 2.82 eV (Fig. S13). Nevertheless, a significant increase of light adsorption in the visible region is observed in the presence of all types of CNTs, even for low CNTs-loadings, e.g. CN-SW1. The enhanced visible light absorption most likely originates from the strong absorption of CNTs in this region. In addition, there might be a contribution from electronic transition due to the coupling of CN with CNTs that increases the surface electric charge of the CN. In the former case, the significant increase of absorption in some nanocomposites (i.e. high loaded materials in Fig. S12) may indicate overloading of CNTs. This may have detrimental effects in photoactivity via competition for light absorption (e.g. shading effect) and/or significant coverage of the CN active phase.

The time profiles of the photocatalytic H_2 evolution activity under solar light irradiation using Pt as co-catalyst is presented in Fig. 3 and S14. No H_2 evolution was detected during blank experiments carried out in the absence of photocatalyst or light irradiation. The observed linearity over a period of 24 h demonstrates the stability of all catalysts under these conditions. Photoactivity is drastically affected by the CNTs content in all three series (Fig. 3A and S14). H_2 evolution shows a rise first followed by a decline with increasing CNTs content. These data do not follow either the BET surface area or the visible light absorption properties of the prepared materials. Considering that surface area plays an important role in photocatalysis, the decrease in photoactivity with increasing surface area may suggest that the enhanced surface area in the composites originates primarily from exposed CNTs that are catalytically inactive. This is clearly observed for the CN-SW*x* and CN-DW*x* series where bigger differences were detected with varying CNTs content. A 3.4 fold increase of H_2 evolution was observed for the CN-SW2 catalyst when compared with the reference CN sample. As a reference reaction, mechanically mixed CN and SWCNTs in amounts identical to the CN-SW2 sample composition (i.e. the most active catalyst) resulted in H_2 production less than the pristine CN. This clearly highlights the importance of the CN in-situ growth in the presence of the CNTs, suggesting the development of a synergy between the individual parts of the composite.

When small amounts of MWCNTs were used to obtain nanocomposites with CN, a small increase in H_2 production is detected for the CN-MW2 catalyst (Fig. S14B) which agrees with previous studies [37]. Further increase of the MWCNTs content resulted in a severe decrease of photoactivity. For example, the H_2 production by the CN-MW4 catalyst was decreased by approximately three times when compared with the CN reference catalyst (Fig. S14B). Recently, an

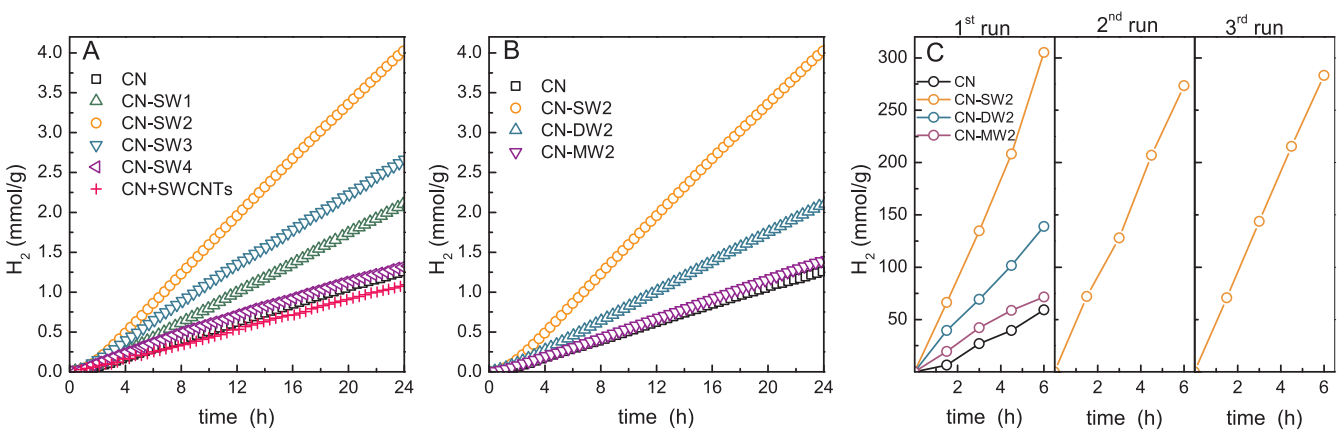

Fig. 3. Photocatalytic H_2 evolution over the prepared nanocomposites under solar (A and B) and pure visible light irradiation (C). Pt (1.5 wt%) was photodeposited in-situ and used as co-catalyst. H_2 evolution over A) the CN-SWx catalysts, the reference CN sample and the physically mixed CN and SWCNTs (CN + SWCNTs) under solar light, B) the nanocomposites containing similar CNTs content but of difference wall number under solar light and C) under pure visible light irradiation (λ > 400 nm). The linearity observed over 24 h of solar light irradiation (A and B) and the consecutive reactions under visible light irradiation (C) verify the stability of the prepared materials under working conditions.

approximately 2 times increase in H_2 photoproduction was reported for MWCNTs/CN composites [29,30]. In these studies functionalized MWCNTs and cyanamide were used instead. Vice versa, She et al. did not observe any improvements for materials developed using melamine and MWCNTs [37]. Therefore, the photocatalytic H_2 evolution is greatly affected by the precursor and the actual conditions used for the development of CNTs/CN nanocomposites.

More importantly, besides the effect on photoactivity of the CNTs content in the nanocomposites, significant differences were detected depending on the wall number of the CNTs. Fig. 3B compares the photocatalytic H_2 production by the most active catalysts of the three series prepared. As it can be observed, photoactivity is increased in the order of SW > DW > MW. The CN-SW2 photocatalyst presented 2 and 3.2 times higher H_2 production than that of CN-DW2 and CN-MW2, respectively, and 3.4 than the pristine CN. CNTs of different wall number differ also in the conductive/semiconductive character [48]. However, a reference reaction performed using only SWCNTs resulted to no H_2 evolution. Therefore, considering that the catalytic conditions are identical and that the CNT content is similar in the three nanocomposites presented in Fig. 3B, the observed difference in activity is strictly attributed to the wall number of the CNTs used. Although previous studies have shown the improved photoactivity of CN when coupled with MWCNTs attributed to the efficient charge migration and separation [30], the data in Fig. 3B clearly suggest that the effect of the CNTs wall number seems significantly more prominent.

A similar trend was observed under pure visible light irradiation ($\lambda > 400$ nm) (Fig. 3C). Under these conditions, the CN-SW2 presented a 5-fold increase in H_2 evolution compared with the pristine CN. The higher activity observed under pure visible light irradiation indicates that the improved light absorption of the composites in the visible region has an impact in photoactivity. An optical charge transfer transition between CNTs and CN may be involved as suggested previously in composites made of TiO_2 and carbon matrix [49]. Consecutive runs under the same conditions performed for the most active catalyst verified the stability of the CNTs/CN nanocomposites.

Different factors contribute to the photocatalytic activity of a semiconductor [50]. Close inspection of the catalytic results reveals that photocatalytic H_2 production does not follow either the specific surface area or the light absorption properties of the prepared nanocomposites. This indicates that a combination thereof and/or other properties control activity. The vital role of the interface in composite materials in charge transfer and separation mechanisms is well established [51]. In the materials developed herein where small amounts of CNTs were used, decreasing the CNTs wall number and keeping constant the CNTs/CN weight ratio leads inevitably to increased hetero-interfaces formed between CNTs and CN. In other words, the hetero-interfaces are expected to be higher in the nanocomposites bearing SWCNTs. This might have an impact in activity by providing more channels for e^- transportation. The decrease of the hetero-interfaces in the composites containing DWCNTs and MWCNTs can be compensated by increasing the CNTs/CN weight ratio. However, increase of the DWCNTs and MWCNTs content results in lower activity (Fig. S14). This observation may indicate that the actual CNTs structure and in particular the CNTs wall number has a direct impact in the photocatalytic process. In addition, the observed increase in H_2 evolution with decreasing CNTs wall number may be affected but is not strictly related to the hetero-interfaces population. Connected pathways and interfacial area between donor and acceptor material have been shown to play critical role in bulk-heterojunction organic solar cells [52]. Considering the similarities of the two processes, a similar effect of the interfacial area is anticipated. However, it does not seem the critical factor controlling the trend observed in photoactivity.

It is well established that among the different factors, both the abundance and stability of photogenerated charges are considered essential for photocatalysis. Herein, in an effort to establish the electronic properties that govern activity, cyclic voltammograms, PL, transient absorption spectroscopy (TAS) and EPR spectra of the prepared catalysts were recorded.

Cyclic voltammograms (Fig. S15) were measured in phosphate-buffered saline (PBS, pH = 7.4) to discover the intrinsic electrochemical behavior of the materials. No special features are detected in accordance with the absence of surface functionalities on the pristine CN, CN-SW2 and CN-DW2. A reduction peak at ca. − 0.6 V was detected probably originating from a defective surface possibly with oxygen [53]. Furthermore, surface-sensitive ferrocyanide-ferricyanide redox couple was used to further investigate the surface morphologies [53–55] by assessment of heterogeneous electron-transfer (HET) rates. An increase in intensity is observed when comparing the nanocomposites with the CN reference sample. This can be indicative of a faster electron transfer rate (k°) in the case of the nanocomposites with respect to the pristine CN with a beneficial effect in catalysis. The observed trend is in line with the catalytic efficiency.

To establish a possible effect of CNTs on charge separation, the steady-state PL spectra of the prepared nanocomposites were recorded (Fig. S16). PL emission originates from the radiative recombination of free charge carriers and has been used to study charge separation efficiency [56]. As evidenced, the PL emission intensity in all nanocomposites is significantly decreased compared with the reference CN sample. These differences indicate that the nanocomposites introduce an additional decay pathway in kinetic competition with radiative recombination. This most likely originates from the transfer of photogenerated electron in the conduction band of CN to the CNTs, preventing a direct recombination of photoexcited electrons and holes. However, the intensity decrease does not follow the catalytic activity trend. This may originate from the wide light absorption due to the presence of the CNTs [30]. However, since short transport pathways of photogenerated electrons to the surface and their stabilization might be of significance, EPR spectroscopy was applied to study these processes and provide quantitative estimation of the photogenerated charges.

EPR spectroscopy is a versatile tool to detect paramagnetic species such as free radicals or e^- in the conduction band of a semiconductor [50]. To analyze the ability of the prepared materials to stabilize photogenerated charges and to observe the total charges formed, in-situ EPR spectroscopy has been applied. EPR spectra of the pure CN and CN/CNTs nanocomposites after UV–visible or pure visible light irradiation are displayed in Fig. S17. All samples exhibited a single symmetric Lorentzian line centered at g 2.0034. An identical EPR signal smaller in intensity was also present under dark conditions and is subtracted from the spectra shown in Fig. S17. The EPR signal centered at 2.0034 increased upon increasing irradiation time. This verifies the formation of paramagnetic centers under light irradiation. The g value suggests that the unpaired electron spin density is delocalized mainly on carbon atoms [57]. The conduction band of CN is formed by carbon 2p orbitals [5]. Similar EPR signals have been previously attributed to unpaired electrons on carbon atoms of aromatic rings within π-bonded nanosized clusters, typical for the heptazine groups of CN [58,59]. It is highlighted that the observed EPR signal does not originate from the CNTs since g-values for pure CNTs are expected to be highly anisotropic, varying between 2.0110 and 2.0206 [60].

A first important observation is that the intensity of the paramagnetic species increased upon either pure visible or UV–visible light irradiation. This observation clearly indicates the formation of photogenerated species, which are associated with photo-excited electrons at the conduction band of CN. In addition, a significant increase of the EPR signal intensity (based on double integration analysis) was detected for the nanocomposites with respect to the reference CN sample. Fig. 4A presents the relative EPR intensity of the nanocomposites taken under UV–visible and pure visible light irradiation normalized to the intensity of the reference CN sample irradiated under similar conditions. The trend of the relative EPR signal intensity shows similarities with the trend of the catalytic activity (compare Fig. 3 *vs.* 4 A). In addition, the nanocomposites bearing SWCNTs presented the highest EPR

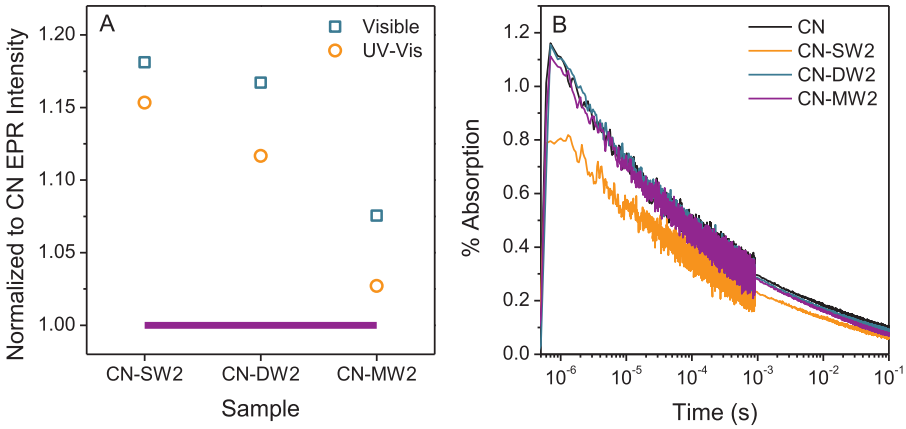

Fig. 4. A) Relative EPR intensity of the signal at $g = 2.0034$ normalized to the pure CN signal intensity for the samples CN-SW2, CN-DW2 and CN-MW2. Samples (80 mg) were irradiated at liquid nitrogen temperature for 20 min under UV–visible light (circles) and $\lambda > 400$ nm (squares). The bar indicates the relative EPR intensity of the reference CN sample. B) Decay kinetics at 900 nm for dispersions of the CN composites in 10% v. of TEOA aqueous solutions. 2 mg/ml of each sample was used, and samples were photoexcited at 355 nm with a fluence of 300 μJ/cm^2.

signal intensity. Under UV–visible light irradiation, the CN-SW2 catalyst presented approximately 16% increased intensity compared with the pure CN. The signal intensity difference was higher when the samples were irradiated under pure visible light. This most likely originates from the improved optical properties of the nanocomposites as revealed with DR-UV–Vis. This explains the higher improvement in H_2 production compared with the pristine CN when the catalysts were irradiated with pure visible light irradiation. Thus, the formation of CNTs/CN nanocomposites helps to optimize the charge formation, suggesting a possible suppression of their recombination.

To further investigate a possible charge transfer pathway between CN and CNTs and to directly monitor photogenerated species in the prepared nanocomposites, we performed diffuse reflectance TAS [61]. TAS is particularly useful to monitor charges populating nonemissive trap states and enables a direct observation of the charge carriers dynamics. Photoexcitation of an aqueous CN dispersion results in the appearance of a long-lived broad photoinduced absorption signal spanning the 550–1100 nm range which decays over microsecond-second timescales (Fig. S18). The decay kinetics roughly shows a power law behavior with exponent $\alpha \sim 0.24$ (Fig. S19), indicative of tail state trapping/detrapping-mediated recombination and consistent with previous investigations of carbon nitrides [62,63]. To establish the nature of the monitored species, we conducted experiments in the presence of chemical scavengers. Adding 10% v. of the hole scavenger TEOA, as used in the photoactivity measurements, results in no change in the spectral shape and amplitude but slightly increases the lifetime of the decay monitored at 900 nm (Figs. S20 and S21). Using 10 mM $AgNO_3$ as an electron scavenger reduces the initial signal amplitude by 33% while the decay kinetics are unaffected (Figs. S21). From these results we assign the observed signal to deeply trapped photogenerated electrons in CN, as recently reported for similar carbon nitride materials [62–64]. We note that these electrons with lifetimes on the order of microseconds and longer are unlikely to participate in charge transfer reactions due to substantial trapping and loss of driving force [62]. Turning to the composite materials, the presence of DWCNTs and MWCNTs does not affect the transient absorption at 900 nm compared to the pure CN in 10% v. TEOA solution (Fig. 4B). Significantly, only the SWCNTs induce a decrease in initial signal amplitude (ca. 27.3%), also seen in the TAS spectra taken at 10 μs (Fig. S18). Productive charge transfer is thought to take place on the sub-μs timescale when photogenerated charges are still in highly reactive states [62]. The decrease in signal amplitude is thus attributed to reactive electron transfer from CN to SWCNTs taking place on the sub-μs timescale prior to substantial trapping and loss of driving force. The TAS results clearly indicate that the electron transfer from CN to CNTs is most efficient in the case of SWCNTs. Most importantly, the electrons transferred correspond to reactive electrons that may participate in the H_2 evolution reaction.

Further insight into the charge dynamics can be gained by combining the EPR and TAS results. This is done in an attempt to estimate the overall charge transfer efficiency. EPR revealed that the abundance of photoinduced electrons is improved in all nanocomposites containing CNTs of different wall number compared with the CN reference material (Fig. 4A). However, this is not expressed in the TAS results. The TAS initial signal amplitude is either the same (i.e. for CN-DW2 and CN-MW2) or lower (i.e. for CN-SW2) (Fig. 4B). As explained above, the loss of CN-SW2 TAS initial signal amplitude (ca. 27.3%) compared with the reference CN is attributed to electron transfer from CN to SWCNTs. However, the fact that the improved electron formation for both CN-DW2 and CN-MW2 (as evidenced by EPR (Fig. 4A)) is not observed by TAS (Fig. 4B) may imply that the additional electrons formed in the nanocomposites compared to the reference CN material have been transferred to the CNTs assuming that recombination rates in the CN domains are similar in the CN and nanocomposite materials (supported by the indistinguishable TAS decay kinetics (Fig. S22)). This is supported by the presence of an optical charge transfer transition between semiconductors and carbon matrix [49]. Based on this, the sum of the improved EPR signal intensity (related to improved charge formation) and the loss of the TAS initial amplitude (related to improved charge separation) may give an estimation of the apparent electron transfer efficiency. This may be expressed as in the following:

$$Apparent\, e^{-}transfer = 1 + \frac{EPR_{NC} - EPR_{CN}}{EPR_{CN}} + \frac{TAS_{CN} - TAS_{NC}}{TAS_{CN}}$$

where EPR_{CN} and EPR_{NC} correspond to the EPR signal intensity of the CN reference and the nanocomposites, and TAS_{CN} and TAS_{NC} to the TAS initial amplitude of the CN reference and the nanocomposite materials, respectively. In other words, the first term on the right side of the equation corresponds to the relative EPR signal intensity increase in the CNTs/CN composites compared with the reference CN while the second to the relative loss of the TAS signal amplitude with respect to the reference CN sample. Both signals correspond to photogenerated electrons. Fig. S23 presents the correlation plot of the calculated apparent electron transfer efficiency *vs.* H_2 evolution. The observed linearity suggests a correlation between the nanocomposites containing CNTs of different wall number and the electron transfer ability. Decreasing the CNTs wall number results in enhanced apparent electron transfer efficiency.

In view of the combined catalytic and spectroscopic study, the effect of the CNTs used for the development of the photocatalysts can now be discussed. The presence of CNTs improved significantly the light absorption properties with a more pronounced effect in photoactivity under visible light irradiation. However, excess of CNTs resulted to detrimental effect in activity. As known, the π-conjugated CNTs can act as efficient electron acceptors due to their high conductivity [31] reducing the e^{-}/h^{+} recombination rates and increasing the probability of the photogenerated charges to participate in redox reactions. Electron equilibration between semiconductors and CNTs through charge transfer and charge storage on the CNTs has been previously proven

[65]. In addition, although the Fermi level in the composites is expected to be less negative than that of the pristine CN and therefore provide lower driving force for the overall reduction reaction, photoactivity of the prepared composites was improved for the optimum CNTs content. It can be therefore concluded that the charge separation through electron transfer and/or electron storage mechanism prevailed.

As proven herein by EPR spectroscopy, the presence of CNTs in the composites increased the overall abundance of photogenerated charges. SWCNTs have a more prominent impact to this end, suggesting that the observed difference in the photocatalytic H_2 evolution is directly correlated to the wall number of the CNTs used for the development of the composite. TAS provided evidence for the presence of a direct charge transport pathway allowing the transfer of reactive electrons from CN to SWCNTs. In addition, the apparent electron transfer efficiency is inversely proportional to the wall number of the CNTs used in the design of the nanocomposites. This explains the improved H_2 evolution in composites bearing SWCNTs. Charge transfer is also known to be a key factor for the efficiency of heterostructures applied in other photo-triggered reactions such as in photovoltaics [66]. In such systems, efficiency is also critically affected by the interfacial area between donor and acceptor material. Similarly, in the present study this is expressed by the number of hetero-interfaces formed within the nanocomposite using CNTs of different wall number. Morphological changes induced by the different CNTs used may also have an impact, since SWCNTs resulted to thinner and smaller CN particles, a factor that shortens the transferring pathway of e^- to reach the surface reducing the probability of recombination. In a similar manner, increase of the wall number of the CNTs may also quench the lifetime of transferred electrons, although this has been suggested to play a minor role in photochemical events in functionalized CNTs [67]. In a scheme like this, increasing the CNTs wall number would result in a diffusive/two-dimensional transport pathway for the electrons on the CNTs. On the contrary, this would be a one-dimensional pathway for the SWCNTs case allowing fast and more efficient electron transport. Therefore, increasing the CNTs wall number may significantly increase the probability of energy relaxation of photogenerated electrons in a manner similar to graphene [38]. In addition, electron transfer within the CNTs walls is expected to be a faster process than the heterogeneous charge transfer at the composites/water interface. Therefore, the CNTs wall number is expected to play an important role in charge transfer properties and, as proven herein, electron transfer from CN to CNTs is more efficient in the case of SWCNTs. This results in an efficient charge separation increasing the number of available charges for H_2 production. Hence, photocatalytic H_2 production is controlled by the CNTs wall thickness which regulates the charge handling properties allowing efficient charge transfer from CN to CNTs.

Based on the above, a schematic illustration of the mechanism suggested is presented in Fig. 5. The abundance and stability of the photogenerated charges increases with decreasing the CNTs wall number, improving the photocatalytic H_2 production. This is mainly attributed to the improved electron transfer from CN to CNTs which is manifested in the ideal case of SWCNTs. Morphology may also contribute to the improved photoactivity. CNTs of few wall number (primarily SWCNTs and to a lesser extent DWCNTs) have greater ability and flexibility to penetrate within the CN nanoplates framework and weaken the interlayer stacking or hydrogen bonding forces resulting in thinner and smaller CN particles. Through this mechanism, the interaction of CN with CNTs is improved, increasing the population of the hetero-interfaces formed within the nanocomposite. Overall, owing to the more efficient electron transfer from CN to CNTs of less wall number, better charge carrier separation is anticipated resulting in improved H_2 photoproduction. This is manifested in the ideal case of SWCNTs.

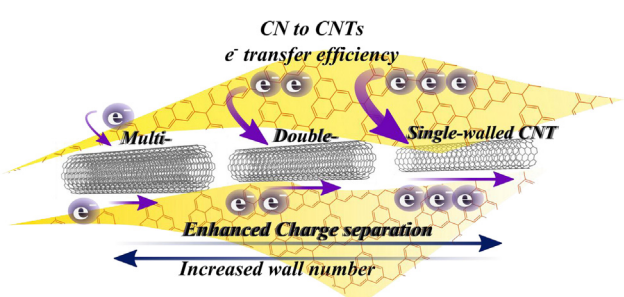

Fig. 5. Schematic illustration of the electron transfer efficiency from CN to CNTs and electron transport pathway within CNTs for composites containing SWCNTs, DWCNTs and MWCNTs. Electron transfer is more efficient in SWCNTs/CN nanocomposites. DWCNTs and MWCNTs provide a two-dimensional transport pathway while SWCNTs a one-dimensional pathway for e^- allowing faster and more efficient charge separation.

3. Conclusion

Nanocomposites developed through the coupling of CN with CNTs of varying wall number where efficiently synthesized and applied in photocatalytic H_2 production. While the presence of CNTs induced some changes in the CN structure, the textural properties of the prepared heterostructures were similar to that of the pristine CN. However, significant difference was observed on photoactivity. The CNTs loading in the final material played crucial role in photoactivity. The optimal CNTs loading was approximately 0.5% for all three composite series prepared. However, the factor that controlled activity is directly correlated with the CNTs wall number. Electron charge transfer from CN to CNTs was inversely proportional to the CNTs wall number. Therefore composites loaded with CNTs of thinner wall presented enhanced H_2 evolution. This was assigned primarily to the CNTs wall number that may affect the charge separation efficiency.

4. Methods

All chemicals were reagent grade and used without further purification. Melamine and triethanolamine (TEOA) were persuaded from Aldrich. Pristine SWCNTs were obtained from Nanointegris (HiPco® Single-Wall Carbon Nanotubes, lot number SP2167, superpure type, diameter: 1.2–1.7 nm, length Range: 100 nm to 4 μm, BET surface area: 400–1000 m^2/g). Pristine DWCNTs were purchased from Nanocyl (lot number: NC2100, DWCNT 90 + % Carbon purity, average diameter: 3.5 nm, average length: 1–10 μm, BET surface area: > 500 m^2/g). Pristine MWCNTs were purchased from Nanostructured & Amorphous Materials (1229YJ 95%, outer diameter 20–30 nm, sverage length: 10–30 μm, BET surface area: > 110 m^2/g).

4.1. Materials synthesis

Pure CN was synthesized via the thermal polycondensation of melamine at 540 °C for 4 h with a heating rate of 5 °C min^{-1}. [9] For the development of the CNTs/ CN nanocomposites, 8.00 g of melamine were added in 400 ml of double distilled water and sonicated for 1 h at room temperature. A specific amount of bare CNTs was added into the above dispersion and the dispersion was further sonicated for 3 h followed by stirring overnight at 80 °C. The powder was filtrated and dried at 70 °C overnight. Finally, the material was placed into an alumina crucible with a cover and heated in air at 540 °C in a muffle furnace for 4 h with a heating rate of 5 °C min^{-1}. The prepared materials were incubated under stirring in DMSO for 4 days, separated with centrifugation and washed with ethanol three times, dried at 70 °C overnight and finally vacuum treated at 90 °C overnight. Three series were prepared using MWCNTs, DWCNTs and SWCNTs. The amount of the CNTs used was 5, 10, 20 and 100 mg, corresponding to a nominal content of 0.0625, 0.125, 0.25 and 1.25 wt% with respect to melamine, respectively. The color of the final nanocomposite changed from yellow

to green and finally dark grey with increasing CNTs content. The nanocomposites are labeled CN-Y*x* where Y indicate the CNTs used (e.g. SW for single-walled) and the increasing *x* value denotes samples with increasing CNTs content. For example, CN-SW2 stands for nanocomposites containing 0.125 wt% SWCNTs as to melamine. CN stands for the pure CN.

4.2. Materials characterization

Thermogravimetric analysis (TGA) was performed with a TGA Q500 (TA Instruments) under N_2 flow, from 100° to 800°C with a heating rate of 10 °C min^{-1}. Nitrogen adsorption-desorption isotherms were obtained at the liquid nitrogen temperature using a Micrometrics ASAP2020 system. Each sample was degassed at 170 °C overnight and the Brunauer-Emmett-Teller (BET) model was used to determine the specific surface area. Fourier transform infrared (FT-IR) spectra in the 4000–400 cm^{-1} region were recorded using KBr pellets with a Perkin Elmer 2000 instrument. Photoluminescence spectra of the prepared catalysts were recorded with a Hitachi F-2500 fluorophotometer. The samples were excited at 360 nm. Fluorescence intensity decay curves were acquired with a time-correlated single photo counting (TCSPC) setup (DeltaFlex, Horiba). Pulsed 404 nm excitation (10 kHz repetition rate) was generated by a laser diode and fluorescence was detected at 455 nm (SPC-650 detector, Horiba). EPR spectra were recorded with a Bruker ER200D instrument operating in the X-band. All spectra were recorded at liquid nitrogen temperature in a double T-type cavity, using diphenyl-picryl-1-hydrazyl (DPPH) as standard (with g = 2.0036) to calibrate the microwave frequency. 80 mg of the samples were placed in a quartz EPR tube and were irradiated for specific period at liquid N_2 with UV–visible or pure visible light ($\lambda > 400$ nm) using a solar simulator (LOT-Oriel) equipped with a 150 W Xe lamp.

Raman spectra were acquired with a Renishaw instrument, model Invia reflex equipped with 532, 633, and 785 nm lasers. XRD patterns were recorded in Bragg-Brentano para-focusing geometry using a Bruker D5000 diffractometer, equipped with Cu Kα anode and graphite monochromator. The XRD data were collected in the angular range 10–80° in 2θ, 0.05° step size and counting time of 5 s per step. The X-ray photoelectron spectroscopy (XPS) analyses were performed with a VGMicrotech ESCA 3000Multilab, equipped with a dual Mg/Al anode. The spectra were excited by the unmonochromatized Al Kα source (1486.6 eV) run at 14 kV and 15 mA. The analyzer was operated in the constant analyzer energy (CAE) mode. For the individual peak energy regions, a pass energy of 20 eV set across the hemispheres was used. Survey spectra were measured at 50 eV pass energy. The sample powders were analyzed as pellets, mounted on a double-sided adhesive tape. Contact of the samples with air was minimized during sample loading. The pressure in the analysis chamber was in the range of 10^{-8} Torr during data collection. The constant charging of the samples was removed by referencing all the energies to the C 1s set at 285.1 eV, arising from the adventitious carbon. The invariance of the peak shapes and widths at the beginning and at the end of the analyses ensured absence of differential charging. Analyses of the peaks were performed with the software CASAXPS. Atomic concentrations were calculated from peak intensity using the sensitivity factors provided with the software. The binding energy values are quoted with a precision of ± 0.15 eV and the atomic percentage with a precision of ± 10%.

Transmission electron microscopy (TEM) measurements were obtained using a FEI Tecnai G2 transmission electron microscope. Atomic Force Microscopy (AFM) measurements were performed using a *Nanoscope V* microscope (*Digital Instruments Metrology Group*, model *MMAFMLN*) in tapping mode in air at room temperature, using standard μmash® SPM probe (NSC15/AIBS) with tip height 12–18 μm, cone angle < 40° (Resonant frequency 325 kHz, force constant of ~ 40 N/m). Image analysis has been performed with *WsXM* software (Nanotec Electronica S. L.) [68]. The accuracy of the AFM diameter determination was improved by tip deconvolution. Considering the diameter of AFM tip and the larger dimensions of particles, we calculated real particle diameter from formula:

$$r_c = r(\cos\theta_0 + (\cos^2\theta_0 + (1+\sin\theta_0)(-1 + (\tan\theta_0/\cos\theta_0) + \tan^2\theta_0))^{1/2})$$

where r is the particle radius, θ_0 is the mean half angle of the tip and r_c is the AFM radius of a particle, as seen in the image [69]. For the preparation of sample surfaces 1 mg of the material was dispersed in 10 ml of EtOH with the assist of sonication and then were spincoated on a SiO_2 surfaces.

UV–visible diffuse reflectance spectroscopy experiments were performed with a PerkinElmer (Lamda 35) spectrophotometer equipped with an integrating sphere assembly with a nominal resolution of 1 nm using $BaSO_4$ as reference. The band gap energies of prepared materials were estimated from their optical absorption edges using the following formula:

$$ahv = B(hv - E_g)^2$$

where hν, α and B represent the excitation energy, absorption coefficient and a constant, respectively. Instead of a, the Kubelka-Munk function was applied in order to eliminate any tailing contribution from the DR-UV–Vis spectra [70]. The following function was applied to convert the absorption spectra:

$$F(R) = \frac{(1-R)^2}{2R}$$

where *R* is the reflectance. The E_g values were estimated from the plot of $F(R)hv^2$ versus energy by extrapolating the linear part.

Diffuse reflectance TAS data were acquired on a home-built setup using 355 nm excitation pulses of 300 μJ/cm^2 from an Nd:YAG laser (OPOTEK Opolette 355 II, 7 ns pulse width). A quartz halogen lamp (Bentham IL1) generated the broadband probe light. Long pass filters were positioned between the lamp and the samples to reduce short wavelength irradiation. An IR filter (5 cm path length cuvette filled with DI water) was also placed before the samples to avoid excessive heating. The probe light was collected in diffuse reflectance mode by a 2″ diameter, 2″ focal length lens and relayed to a monochromator to select the probe wavelength. Another long pass filter was placed at the entrance of the monochromator to reject scattered laser light. The collected light was focused onto a Si photodiode detector (Hamamatsu S3071) to monitor changes in reflectance. Sub-ms data were processed by an electronic amplifier (Costronics) and recorded on an oscilloscope. Data on the ms timescale were simultaneously recorded by a DAQ card (National Instruments). Acquisitions were triggered by scatter from the laser excitation measured by a photodiode (Thorlabs DET10A). Each acquisition averaged 32 laser pulses and were processed using home-built LabVIEW software. The measurements were performed on argon-purged aqueous dispersions (2 mg/ml of material).

4.3. Photocatalytic activity evaluation

Photocatalytic hydrogen production was evaluated under simulated sunlight irradiation using a solar simulator (LOT-Oriel) equipped with a 150 W Xe lamp and an Atmospheric Edge Filter to cut-off UV photons below 300 nm. This results in a surface power density of ~ 25 mW cm^{-2} in the UV range (300–400 nm) and ~ 180 mW cm^{-2} in the visible range (400–1000 nm), approaching the conditions used in a solar concentrator. Flow reaction conditions were applied for the experiments using simulated sunlight irradiation. In a Teflon-lined photoreactor described elsewhere [4], 60 mg of the prepared materials were suspended into 80 ml of a 10 v% triethanolamine (TEOA) aqueous solution. 1.5 wt% of Pt nanoparticles used as co-catalyst were photo-deposited in-situ by adding $Pt(NO_3)_2$. The reaction temperature was maintained at 25 °C by mean of a cryostat and air was removed from the reaction mixture prior to irradiation by purging with argon (15 ml min^{-1}) for 40 min. Evolved gaseous products were detected on-line by an Agilent 7890 gas chromatographer equipped with a Carboxen 1010

PLOT (Supelco, 30 m × 0.53 mm ID, 30 μm film) column using Ar as carrier followed by a Thermal Conductivity Detector (TCD) and DB-225 ms column (J&W, 60 m × 0.32 mm ID, 20 μm film) using He as carrier followed by a mass spectrometer (MS) HP 5975C. Catalytic experiments were also contacted under pure visible light irradiation using a 400 nm cut-off filter. For these experiments, reactions under batch conditions were performed and evolved gases were sampled periodically.

Acknowledgment

K.C.C. acknowledges the TALENTS FVG Programme for a Post-doctoral fellowship funded from the European Social Fund (Operational Programme 2007–2013, Objective 2 Regional Competitiveness and Employment, Axis 5 Transnational cooperation, TALENTS FVG Programme). R.G. thanks the Fonds de recherche – Nature et technologies du Québec for a postdoctoral fellowship.

Supporting information

Supporting information data containing TGA, XRD, FT-IR, Raman, XPS, N_2 adsorption-desorption isotherms, pore size distribution, AFM, DR-UV–Vis, H_2 evolution, cyclic voltammetry, PL, EPR and TAS data are available.Funding sources

This work was partially supported by the University of Trieste through the FRA2015 scheme and the Engineering and Physical Science Research Council through the First Grant scheme (EP/N024206/1) and via a Departmental Training Partnership grant, the Engineering and Physical Science Research Council through the First Grant scheme (EP/N024206/1), ERC AdG Intersolar Grant (291482), and via a Departmental Training Partnership grant.

References

[1] Y. Ma, X. Wang, Y. Jia, X. Chen, H. Han, C. Li, Titanium dioxide-based nanomaterials for photocatalytic fuel generations, Chem. Rev. 114 (2014) 9987–10043.
[2] K.C. Christoforidis, P. Fornasiero, Photocatalytic hydrogen production: a rift into the future energy supply, ChemCatChem 9 (2017) 1523–1544.
[3] Y.P. Xie, Z.B. Yu, G. Liu, X.L. Ma, H.-M. Cheng, CdS–mesoporous ZnS core–shell particles for efficient and stable photocatalytic hydrogen evolution under visible light, Energy Environ. Sci. 7 (6) (2014) 1895.
[4] G. Carraro, C. Maccato, A. Gasparotto, T. Montini, S. Turner, O.I. Lebedev, V. Gombac, G. Adami, G. Van Tendeloo, D. Barreca, P. Fornasiero, Enhanced hydrogen production by photoreforming of renewable oxygenates through nanostructured Fe_2O_3 polymorphs, Adv. Funct. Mater. 24 (3) (2014) 372–378.
[5] X. Wang, K. Maeda, A. Thomas, K. Takanabe, G. Xin, J.M. Carlsson, K. Domen, M. Antonietti, A metal-free polymeric photocatalyst for hydrogen production from water under visible light, Nat. Mater. 8 (1) (2009) 76–80.
[6] V.S. Vyas, V.W.-H. Lau, B.V. Lotsch, Soft photocatalysis: organic polymers for solar fuel production, Chem. Mater. 28 (15) (2016) 5191–5204.
[7] W.J. Ong, L.L. Tan, Y.H. Ng, S.T. Yong, S.P. Chai, Graphitic carbon nitride (g-C3N4)-based photocatalysts for artificial photosynthesis and environmental remediation: are we a step closer to achieving sustainability? Chem. Rev. 116 (12) (2016) 7159–7329.
[8] S. Cao, J. Yu, g-C3N4-based photocatalysts for hydrogen generation, J. Phys. Chem. Lett. 5 (12) (2014) 2101–2107.
[9] K.C. Christoforidis, T. Montini, E. Bontempi, S. Zafeiratos, J.J.D. Jaén, P. Fornasiero, Synthesis and photocatalytic application of visible-light active β-Fe2O3/g-C3N4 hybrid nanocomposites, Appl. Catal. B: Environ. 187 (2016) 171–180.
[10] Y. Zheng, L. Lin, B. Wang, X. Wang, Graphitic carbon nitride polymers toward sustainable photoredox catalysis, Angew. Chem. Int. Ed. Engl. 54 (44) (2015) 12868–12884.
[11] Z. Zhao, Y. Sun, F. Dong, Graphitic carbon nitride based nanocomposites: a review, Nanoscale 7 (1) (2015) 15–37.
[12] J. Zhang, J. Sun, K. Maeda, K. Domen, P. Liu, M. Antonietti, X. Fu, X. Wang, Sulfur-mediated synthesis of carbon nitride: band-gap engineering and improved functions for photocatalysis, Energy Environ. Sci. 4 (3) (2011) 675–678.
[13] Q. Liang, Z. Li, Z.-H. Huang, F. Kang, Q.-H. Yang, Holey graphitic carbon nitride nanosheets with carbon vacancies for highly improved photocatalytic hydrogen production, Adv. Funct. Mater. 25 (44) (2015) 6885–6892.
[14] Q. Han, B. Wang, Y. Zhao, C. Hu, L. Qu, A. Graphitic-C3N4, "Seaweed" architecture for enhanced hydrogen evolution, Angew. Chem. Int. Ed. Engl. 54 (39) (2015) 11433–11437.
[15] S. Tonda, S. Kumar, S. Kandula, V. Shanker, Fe-doped and -mediated graphitic carbon nitride nanosheets for enhanced photocatalytic performance under natural sunlight, J. Mater. Chem. A 2 (19) (2014) 6772.
[16] J. Zhang, M. Zhang, C. Yang, X. Wang, Nanospherical carbon nitride frameworks with sharp edges accelerating charge collection and separation at a soft photocatalytic interface, Adv. Mater. 26 (24) (2014) 4121–4126.
[17] Y. Wang, X. Wang, M. Antonietti, Y. Zhang, Facile one-pot synthesis of nanoporous carbon nitride solids by using soft templates, ChemSusChem 3 (4) (2010) 435–439.
[18] S. Bai, X. Wang, C. Hu, M. Xie, J. Jiang, Y. Xiong, Two-dimensional g-C(3)N(4): an ideal platform for examining facet selectivity of metal co-catalysts in photocatalysis, Chem. Commun. 50 (46) (2014) 6094–6097.
[19] Q. Xiang, J. Yu, M. Jaroniec, Preparation and enhanced visible-light photocatalytic h2-production activity of graphene/C3N4Composites, J. Phys. Chem. C 115 (15) (2011) 7355–7363.
[20] W.J. Ong, L.L. Tan, S.P. Chai, S.T. Yong, Graphene oxide as a structure-directing agent for the two-dimensional interface engineering of sandwich-like graphene-g-C3N4 hybrid nanostructures with enhanced visible-light photoreduction of CO_2 to methane, Chem. Commun. 51 (5) (2015) 858–861.
[21] Y. Zhao, F. Zhao, X. Wang, C. Xu, Z. Zhang, G. Shi, L. Qu, Graphitic carbon nitride nanoribbons: graphene-assisted formation and synergic function for highly efficient hydrogen evolution, Angew. Chem. Int. Ed. Engl. 53 (50) (2014) 13934–13939.
[22] J. Liu, Y. Liu, N. Liu, Y. Han, X. Zhang, H. Huang, Y. Lifshitz, S.-T. Lee, Zhong, J. Kang, Z. Metal-free, efficient photocatalyst for stable visible water splitting via a two-electron pathway, Science 347 (2015) 970–974.
[23] S. Fang, Y. Xia, K. Lv, Q. Li, J. Sun, M. Li, Effect of carbon-dots modification on the structure and photocatalytic activity of g-C3N4, Appl. Catal. B: Environ. 185 (2016) 225–232.
[24] X. Bai, L. Wang, Y. Wang, W. Yao, Y. Zhu, Enhanced oxidation ability of g-C3N4 photocatalyst via C60 modification, Appl. Catal. B: Environ. 152–153 (2014) 262–270.
[25] H. Sun, G. Zhou, Y. Wang, A. Suvorova, S. Wang, A new metal-free carbon hybrid for enhanced photocatalysis, ACS Appl. Mater. Interfaces 6 (19) (2014) 16745–16754.
[26] Y. Xu, H. Xu, L. Wang, J. Yan, H. Li, Y. Song, L. Huang, G. Cai, The CNT modified white C3N4 composite photocatalyst with enhanced visible-light response photoactivity, Dalton Trans. 42 (21) (2013) 7604–7613.
[27] J. Zhang, M. Zhang, L. Lin, X. Wang, Sol processing of conjugated carbon nitride powders for thin-film fabrication, Angew. Chem. Int. Ed. Engl. 54 (21) (2015) 6297–6301.
[28] Y. Zhong, J. Yuan, J. Wen, X. Li, Y. Xu, W. Liu, S. Zhang, Y. Fang, Earth-abundant NiS co-catalyst modified metal-free mpg-C3N4/CNT nanocomposites for highly efficient visible-light photocatalytic H2 evolution, Dalton Trans. 44 (41) (2015) 18260–18269.
[29] A. Suryawanshi, P. Dhanasekaran, D. Mhamane, S. Kelkar, S. Patil, N. Gupta, S. Ogale, Doubling of photocatalytic H2 evolution from g-C3N4 via its nanocomposite formation with multiwall carbon nanotubes: electronic and morphological effects, Int. J. Hydrog. Energy 37 (12) (2012) 9584–9589.
[30] Y. Chen, J. Li, Z. Hong, B. Shen, B. Lin, B. Gao, Origin of the enhanced visible-light photocatalytic activity of CNT modified g-C3N4 for H2 production, Phys. Chem. Chem. Phys. 16 (17) (2014) 8106–8113.
[31] L. Ge, C. Han, Synthesis of MWNTs/g-C3N4 composite photocatalysts with efficient visible light photocatalytic hydrogen evolution activity, Appl. Catal. B: Environ. 117–118 (2012) 268–274.
[32] Y. Gong, J. Wang, Z. Wei, P. Zhang, H. Li, Y. Wang, Combination of carbon nitride and carbon nanotubes: synergistic catalysts for energy conversion, ChemSusChem 7 (8) (2014) 2303–2309.
[33] T.Y. Ma, S. Dai, M. Jaroniec, S.Z. Qiao, Graphitic carbon nitride nanosheet–carbon nanotube three-dimensional porous composites as high-performance oxygen evolution electrocatalysts, Angew. Chem. Int. Ed. Engl. 53 (28) (2014) 7281–7285.
[34] A.K. Geim, Graphene: status and prospects, Science (2009) 324.
[35] M. Melchionna, M. Prato, P. Fornasiero, Mix and match metal oxides and nanocarbons for new photocatalytic frontiers, Catal. Tod. 277 (2016) 202–213.
[36] D. McAteer, Z. Gholamvand, N. McEvoy, A. Harvey, E. O'Malley, G.S. Duesberg, J.N. Coleman, Thickness dependence and percolation scaling of hydrogen production rate in MoS2 nanosheet and nanosheet-carbon nanotube composite catalytic electrodes, ACS Nano 10 (1) (2016) 672–683.
[37] X. She, J. Wu, H. Xu, Z. Mo, J. Lian, Y. Song, L. Liu, D. Du, H. Li, Enhancing charge density and steering charge unidirectional flow in 2D non-metallic semiconductor-CNTs-metal coupled photocatalyst for solar energy conversion, Appl. Catal. B: Environ. 202 (2017) 112–117.
[38] C.C. Kuo, C.H. Chen, Graphene thickness-controlled photocatalysis and surface enhanced Raman scattering, Nanoscale 6 (21) (2014) 12805–12813.
[39] P.R. Bandaru, Electrical properties and applications of carbon nanotube structures, J. Nanosci. Nanotechnol. 7 (4–5) (2007) 1239–1267.
[40] A.A. Green, M.C. Hersam, Properties and application of double-walled carbon nanotubes sorted by outer-wall electronic type, ACS Nano 5 (2) (2011) 1459–1467.
[41] Y. Zheng, J. Liu, J. Liang, M. Jaroniec, S.Z. Qiao, Graphitic carbon nitride materials: controllable synthesis and applications in fuel cells and photocatalysis, Energy Environ. Sci. 5 (5) (2012) 6717.
[42] S. Yang, Y. Gong, J. Zhang, L. Zhan, L. Ma, Z. Fang, R. Vajtai, X. Wang, P.M. Ajayan, Exfoliated graphitic carbon nitride nanosheets as efficient catalysts for hydrogen

evolution under visible light, Adv. Mater. 25 (17) (2013) 2452–2456.
[43] J.R. Holst, E.G. Gillan, From triazines to heptazines: deciphering the local structure of amorphous nitrogen-rich carbon nitride materials, J. Am. Chem. Soc. 130 (23) (2008) 7373–7379.
[44] E.E. J., O. C. M.; Eibergen, S.K. Doorn, Chiral selectivity in the charge-transfer bleaching of single-walled carbon-nanotube spectra, Nat. Mater. 4 (5) (2005) 412–418.
[45] P. Puech, E. Flahaut, A. Bassil, T. Juffmann, F. Beuneu, W.S. Bacsa, Raman bands of double-wall carbon nanotubes: comparison with single- and triple-wall carbon nanotubes, and influence of annealing and electron irradiation, J. Raman Spectrosc. 38 (6) (2007) 714–720.
[46] A.M. Rao, P.C. Eklund, S. Bandow, A. Thess, R.E. Smalley, Evidence for charge transfer in doped carbon nanotube bundles from Raman scattering, Nature 388 (1997) 257–259.
[47] R. Kitaura, N. Imazu, K. Kobayashi, H. Shinohara, Fabrication of metal nanowires in carbon nanotubes via versatile nano-template reaction, Nano Let. 8 (2008) 693–699.
[48] L. Yu, C. Shearer, J. Shapter, Recent development of carbon nanotube transparent conductive films, Chem. Rev. 116 (22) (2016) 13413–13453.
[49] L. Zhao, X. Chen, X. Wang, Y. Zhang, W. Wei, Y. Sun, M. Antonietti, M.M. Titirici, One-step solvothermal synthesis of a carbon@TiO(2) dyade structure effectively promoting visible-light photocatalysis, Adv. Mater. 22 (30) (2010) 3317–3321.
[50] K.C. Christoforidis, M. Fernández-García, Photoactivity and charge trapping sites in copper and vanadium doped anatase TiO2 nano-materials, Catal. Sci. Technol. 6 (4) (2016) 1094–1105.
[51] A. Crake, K.C. Christoforidis, A. Kafizas, S. Zafeiratos, C. Petit, CO2 capture and photocatalytic reduction using bifunctional TiO2 /MOF nanocomposites under UV–vis irradiation, Appl. Catal. B: Environ. 210 (2017) 131–140.
[52] A.J. Heeger, 25th anniversary article: bulk heterojunction solar cells: understanding the mechanism of operation, Adv. Mater. 26 (1) (2014) 10–27.
[53] Y.T. Yew, C.S. Lim, A.Y.S. Eng, J. Oh, S. Park, M. Pumera, ChemPhysChem 17 (2016) 481.
[54] C.G. Zoski, Handbook of Electrochemistry, Elsevier, Amsterdam, 2007.
[55] S.M. Tan, H.L. Poh, Z. Sofer, M. Pumera, Analyst 138 (2013) 4885.
[56] K.C. Christoforidis, M. Melchionna, T. Montini, D. Papoulis, E. Stathatos, S. Zafeiratos, E. Kordouli, P. Fornasiero, Solar and visible light photocatalytic enhancement of halloysite nanotubes/g-C3N4 heteroarchitectures, RSC Adv. 6 (89) (2016) 86617–86626.
[57] K.C. Christoforidis, S. Un, Y. Deligiannakis, High-field 285 GHz electron paramagnetic resonance study of indigenous radicals of humic acids, J. Phys. Chem. A 111 (2007) 11860–11866.
[58] J. Zhang, G. Zhang, X. Chen, S. Lin, L. Mohlmann, G. Dolega, G. Lipner, M. Antonietti, S. Blechert, X. Wang, Co-monomer control of carbon nitride semiconductors to optimize hydrogen evolution with visible light, Angew. Chem. Int. Ed. Engl. 51 (13) (2012) 3183–3187.
[59] Y. Cui, Z. Ding, X. Fu, X. Wang, Construction of conjugated carbon nitride nanoarchitectures in solution at low temperatures for photoredox catalysis, Angew. Chem. Int. Ed. Engl. 51 (47) (2012) 11814–11818.
[60] T. Tsoufis, A. Ampoumogli, D. Gournis, V. Georgakilas, L. Jankovic, K.C. Christoforidis, Y. Deligiannakis, A. Mavrandonakis, G.E. Froudakis, E. Maccallini, P. Rudolf, A. Mateo-Alonso, M. Prato, Direct observation of spin-injection in tyrosinate-functionalized single-wall carbon nanotubes, Carbon 67 (2014) 424–433.
[61] F. Wilkinson, Diffuse reflectance flash photolysis, J. Chem. Soc. Faraday Trans. 82 (12) (1986) 2073–2081.
[62] R. Godin, Y. Wang, M.A. Zwijnenburg, J. Tang, J.R. Durrant, Time-resolved spectroscopic investigation of charge trapping in carbon nitrides photocatalysts for hydrogen generation, J. Am. Chem. Soc. 139 (14) (2017) 5216–5224.
[63] J.J. Walsh, C. Jiang, J. Tang, A.J. Cowan, Photochemical CO_2 reduction using structurally controlled g-C3N4, Phys. Chem. Chem. Phys. 18 (36) (2016) 24825–24829.
[64] R. Kuriki, H. Matsunaga, T. Nakashima, K. Wada, A. Yamakata, O. Ishitani, K. Maeda, Nature-inspired, highly durable CO_2 reduction system consisting of a binuclear Ruthenium(II) complex and an organic semiconductor using visible light, J. Am. Chem. Soc. 138 (15) (2016) 5159–5170.
[65] A. Kongkanand, P.V. Kamat, Electron storage in single wall carbon nanotubes. Fermi level equilibration in semiconductor–SWCNT suspensions, ACS Nano 1 (1) (2007) 13–21.
[66] G. Yu, J. Gao, J.C. Hummelen, F. Wudl, A.J. Heeger, Polymer photovoltaic cells: enhanced efficiencies via a network of internal donor-acceptor heterojunctions, Science 270 (5243) (1995) 1789–1791.
[67] R. Martín, F.J. Céspedes-Guirao, M. de Miguel, F. Fernández-Lázaro, H. García, Á. Sastre-Santos, Single- and multi-walled carbon nanotubes covalently linked to perylenebisimides: synthesis, characterization and photophysical properties, Chem. Sci. 3 (2) (2012) 470–475.
[68] WSXM: A software for scanning probe microscopy and a tool for nanotechnology. Rev. Sci. Instrum., 2007, vol. 78(1), p. 013705.
[69] M. Rasa, B.W.M. Kuipers, A.P. Philipse, Atomic force microscopy and magnetic force microscopy study of model colloids, J. Colloid Interf. Sci. 250 (2) (2002) 303–315.
[70] K.C. Christoforidis, A. Sengele, V. Keller, N. Keller, Single-step synthesis of SnS(2) nanosheet-decorated TiO(2) anatase nanofibers as efficient photocatalysts for the degradation of gas-phase diethylsulfide, ACS Appl. Mater. Interfaces 7 (2015) 19324–19334.

Dr Konstantinos Christoforidis obtained his PhD from the University of Ioannina (Greece). He is currently Assistant Professor in the Department of Environmental Engineering, Democritus University of Thrace, Greece. His research focuses on the development of photo-activated, multifunctional nanomaterials applied in water splitting, CO_2 photoreduction and environmental depollution, elucidating key materials properties that govern photochemical processes in such applications.

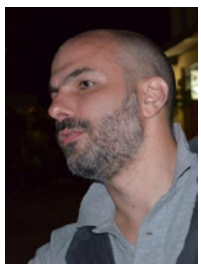

Dr Zois Syrgiannis is a Researcher at the University of Trieste (Italy). He studied in Greece (University of Ioannina) Chemistry where also got his MSc. He obtained his Ph.D. at the University of Erlangen-Nuremberg (Germany), under the supervision of Prof. Andreas Hirsch. He carried out postdoctoral research at the University of Trieste (Italy) and at the IMT-CNR (Padua, Italy), (supervisors: Prof. Mauricio Prato and Prof. Marcella Bonchio). Syrgiannis' research interests concern the chemical manipulation of carbon nanomaterials and the synthesis of organized supramolecular structures. In 2016 he was awarded from the Italian Chemical Society with the Medaglia Giacomo Ciamician for his contribution in the field of Carbon Nanomaterials.

Dr Valeria La Parola is a researcher at the Institute of Nanostructured Materials since 2008. Her main interests are the synthesis and characterization of materials as heterogeneous catalysts for environmental reactions. Studied materials are based on supported metals on inert or reducible oxides or supported metals on carbon nanostructures. Main expertises are on characterization techniques such as nitrogen physisorption, temperature programmed reaction, X-Ray diffraction and X-ray Photoelectronic Spectroscopy. The studied reactions are mainly in gas phase at atmospheric pressure with a focus on methane reforming reactions. Lately she starts working in transesterification reaction for biodiesel production and biomass upgrading

Dr Tiziano Montini received his Ph.D. in 2006 at the University of Trieste (Italy). After a postdoctoral fellowship, he was appointed as an assistant professor in 2014 and associate professor in 2017 at the University of Trieste. In 2012, he was awarded with the "Alfredo Di Braccio" prize by the Accademia Nazionale dei Lincei and the 4th Junior Research Award by the European Rare-Earth and Actinide Society. In 2016 he was the recipient of the Nasini gold medal for his contribution in Inorganic Chemistry.

Dr Camille Petit is based in the Chemical Engineering Department at Imperial where she leads the Multifunctional Nanomaterials Laboratory. Her research interests broadly encompass the development of porous nanomaterials for applications relevant to the energy and environmental sectors. Specifically, she focuses on the synthesis, characterization and testing of metal-organic frameworks (MOFs)- and nitride-based nanomaterials for gas and liquid separations as well as photocatalysis. Recently, she received the 2017 AIChE's 35 under 35 award, the 2017 IOM3 Silver Medal in 'recognition of an outstanding contribution from an early career researcher to a field of interest within the Materials sector'.

Professor Elias Stathatos is the Head of the Nanotechnology and Advanced Materials Laboratory at Technological Educational Institute of Western Greece. He has more than 120 publications in peer reviewed journals, 65 proceedings papers and 6 book chapters which are recognized of more than 5000 citations. He is also co-investigator in five patents and editorial board member at four ISI Journals. His research interests include synthesis of nanostructured semiconductors and conversion of solar into electrical energy using dye-sensitized solar cells and perovskite solar cells. He is also interested in photocatalytic destruction of several organic pollutants over semiconductor nanoparticles.

Dr Robert Godin's research interests are centered in photochemistry and optical spectroscopy. After completing a Ph.D. on the topic of single molecule imaging of redox processes, in 2015 he joined Prof. Durrant's group as a FQRNT postdoctoral research associate to study solar energy conversion technologies. Currently his main focus is the study of promising carbon-based photocatalytic systems, including carbon nitrides and carbon dots, for the production of solar fuels. He has gained an expertise in transient absorption spectroscopy, and uses this powerful tool to better understand key photochemical processes such as charge trapping and charge accumulation.

Professor James Durrant is Professor of Photochemistry in the Department of Chemistry, Imperial College London and Sêr Cymru Solar Professor, College of Engineering, University of Swansea. His research addresses the photochemistry of new materials for solar energy conversion – targeting both solar cells (photovoltaics) and solar to fuel (i.e.: artificial photosynthesis). It is based around employing transient optical and optoelectronic techniques to address materials function, and thereby elucidate design principles which enable technological development. He has published over 400 research papers and 5 patents, and was elected to a Fellow of the Royal Society in 2017.

Professor Maurizio Prato is Professor of Organic Chemistry at the University of Trieste and Ikerbasque Research Professor at CIC BiomaGUNE, Spain. He was the recipient of an ERC Advanced Research Grant, European Research Council, in 2008 and became a Member of the National Academy of Sciences (Accademia Nazionale dei Lincei) in 2010. His research focuses on the synthesis of novel functional materials, for applications in materials science and nanomedicine. Currently, he attempts to transfer the properties of these new materials into applications, which include spinal cord repair, splitting of water, and reduction of carbon dioxide into useful chemicals.

Professor Paolo Fornasiero received his Ph.D. in heterogeneous catalysis in 1997 and is full professor in Inorganic Chemistry at the University of Trieste. He received the Nasini Gold medal in 2005 for his contribution in Inorganic Chemistry and the Chiusoli Gold medal in 2013 for his studies in catalysis by the Italian Chemical Society. In 2016, he received the Heinz Heinemann Award for his contribution to catalyst science and technology from the International Association of Catalysis Societies. In 2017, he delivered the Rudolf Zahradník honorary lecture (Czech Republic). In 2018, he was the recipient of the Kramer Award and of a Visiting Scientist Fellowship by the Chinese Academy of Science.